Submitted to

32nd International Conference on High Energy Physics, ICHEP04, August 16, 2004, Beijing
Abstract: **5-0166**
Parallel Session **5**

www-h1.desy.de/h1/www/publications/conf/conf_list.html

Inclusive Production of D^+, D^0, D_s^+ and D^{*+} Mesons in Deep Inelastic Scattering at HERA

H1 Collaboration

Abstract

Inclusive production cross sections are measured in deep inelastic scattering at HERA for meson states composed of a charm quark and a light antiquark or the charge conjugate. The measurements cover the kinematic region of photon virtuality $2 < Q^2 < 100$ GeV^2, inelasticity $0.05 < y < 0.7$, D meson transverse momenta $p_t(D) \geq 2.5$ GeV and pseudo-rapidity $|\eta(D)| \leq 1.5$. The identification of the D-meson decays and the reduction of the combinatorial background profit from the reconstruction of displaced secondary vertices by means of the H1 silicon vertex detector. The production of charmed mesons containing the light quarks u, d and s is found to be compatible with a description in which the hard scattering is followed by a factorisable and universal hadronisation process.

1 Introduction

The production of heavy quarks in deep inelastic positron-proton interactions at HERA proceeds almost exclusively via photon-gluon fusion, where a photon coupling to the incoming positron interacts with a gluon in the proton to form a charm-anticharm pair (figure 1). Measurements of differential charm production cross sections [1–5] are well reproduced by a description based on perturbative QCD (pQCD). In this framework cross sections $\mathrm{d}\sigma$ for D mesons (bound $c\bar{q}$ states of charm quarks with light antiquarks) can be computed [6–11] by convoluting the parton level hard scattering cross section $\mathrm{d}\hat{\sigma}$ with a fragmentation function $D_D^{(c)}(z)$:

$$\mathrm{d}\sigma(p) \;=\; \int \mathrm{d}z \;\; D_D^{(c)}(z) \cdot \mathrm{d}\hat{\sigma}(p/z) \quad . \tag{1}$$

The cross section $\mathrm{d}\hat{\sigma}$ here describes the hard scattering process $(ep \rightarrow e'cX')$ and the perturbative evolution from the c-quark production scale down to a scale of order of the heavy quark mass m_c [12]. The non-perturbative part of the hadronisation, $D_D^{(c)}(z)$, accounts for the transition of an on-shell quark c of momentum p/z into a hadron D carrying a fraction z of the quark momentum.

This factorisation ansatz can be shown to hold in the asymptotic limit of large production scales [13]. It assumes that the non-perturbative component $D_D^{(c)}(z)$ is independent both of the hard scattering process, e.g. $ee-, ep-$ or $pp-$scattering, and of the scale at which the charm quark is produced. These properties are collectively referred to as "universality" [11, 12, 14, 15]. It has been argued [12, 16] that the assumptions of universality may not hold and that in fact different production processes may be sensitive to different aspects of fragmentation.

Conventionally the shape of $D_D^{(c)}(z)$ is taken to be identical for all primary produced D-mesons, and its normalisation accounts for the abundance of the respective meson D. A well-known parametrisation of this shape is the Peterson function [17] with a suitably chosen normalisation factor n_D

$$D_D^{(c)}(z) \;=\; \frac{n_D}{z[1 - 1/z - \epsilon_c/(1-z)]^2} \quad . \tag{2}$$

The so-called "Peterson parameter" ϵ_c measures the hardness of the hadronisation. In practice, it is extracted from charm spectra measured predominantly at e^+e^- colliders [12].

In this paper the universality ansatz is explored in deep inelastic ep-scattering at HERA. For this purpose production cross sections are measured for the charmed meson state D^+, D^0, D_s^+ and D^{*+}, containing the light quarks u, d and s. The final state requirements differ only in the light quark content or the spin of the charmed meson. For light quark fragmentation the occurrence of different quark flavours in the fragmentation process can be described by isospin relations and probabilistic quark selection factors. While corresponding charm quark fragmentation results are available from other scattering processes [12, 18–20] it is interesting to verify whether

the relations established for light quarks can be extended to mesons containing heavy quarks produced in ep scattering at HERA.

In this analysis the signals of D mesons are enhanced with respect to background processes by exploiting their lifetimes. The displaced secondary decay vertices of the D-mesons are reconstructed from the daughter particle tracks, which are measured with high precision in the H1 central silicon tracker. A common detection method can thus be applied to all four charmed meson states.

2 Experimental Aspects and Data Analysis

The data were collected in 1999 and 2000 with the H1 detector at HERA and correspond to an integrated luminosity of 47.8 ± 0.7 pb^{-1} of e^+p interactions at a centre of mass energy $\sqrt{s} = 319$ GeV. The analysis covers the kinematic region of photon virtuality $2 < Q^2 < 100$ GeV^2, inelasticity $0.05 < y < 0.7$ and D meson transverse momentum and pseudorapidity[1] $p_t(D) \geq 2.5$ GeV and $|\eta(D)| \leq 1.5$. The charmed mesons are detected through their decay products in the decay channels[2] $D^+ \to K^-\pi^+\pi^+$, $D^0 \to K^-\pi^+$, $D_s^+ \to \phi\pi^+ \to (K^+K^-)\pi^+$ and $D^{*+}(2010) \to D^0\pi^+ \to (K^-\pi^+)\pi^+$.

2.1 Detector and Simulation

The H1 detector and its trigger capabilities are described in detail elsewhere [21]. Charged particles are measured by a set of central tracking devices including two cylindrical jet drift chambers (CJC) [22, 23], mounted concentrically around the beam-line inside a homogeneous magnetic field of 1.15 T. They provide particle charge and transverse momentum measurements in the polar angle range $20^\circ < \theta < 160^\circ$. Further drift chambers provide accurate measurements of the z-coordinates.

These central tracking devices are complemented by the central silicon tracker (CST) [24], which consists of two cylindrical layers of silicon strip detectors with active lengths of 35.6 cm surrounding the beam pipe at radii of 57.5 mm and 97 mm from the beam axis. The double-sided strip detectors measure r-ϕ and z coordinates with resolutions of 12 μm and 25 μm, respectively. Average hit efficiencies are 97 (92)% for r-ϕ (z) strips. In this analysis the measurements of the z-coordinates are not used for the secondary vertex determination. When extrapolated to the interaction region, the coordinate perpendicular to a track in the transverse plane has a resolution of 33 μm $\oplus$ 90 μm$/p_t$[GeV] for tracks with CST hits in both layers. The first term represents the intrinsic resolution and includes the uncertainty on the CST alignment. The second term accounts for the contribution from multiple scattering.

One double layer of cylindrical multi-wire proportional chambers (MWPC [25]) with pad readout for triggering purposes is positioned between the CST and the CJC, and another between the two jet chambers. The backward region of H1 is equipped with a lead/scintillating

[1] In the following, the coordinate system used has its origin at the nominal e^+p interaction point and its z-axis in the outgoing proton direction. Polar angles, θ, are measured with respect to the z direction. The pseudorapidity is defined as $\eta = -\ln\tan(\theta/2)$.

[2] The charge conjugate states are always implicitly included.

fibre "Spaghetti" Calorimeter (SpaCal) [26], which is optimized for the detection of the scattered positron in the DIS kinematic range considered here. It consists of an electromagnetic and a more coarsely segmented hadronic section. An eight-layer drift chamber (BDC [27]), mounted in front of the SpaCal, is used to reject neutral particle background. The ep luminosity is determined by measuring the QED bremsstrahlung $(ep \to ep\gamma)$ event rate by tagging the photon in a photon detector located at $z = -103$ m.

Corrections for detector effects are evaluated using detailed Monte Carlo simulations. Charm and beauty electroproduction events are generated according to Leading Order (LO) QCD matrix elements with the AROMA 2.2 [28] program and are combined with parton showering in the JETSET [29] program. The beauty cross section is enhanced by a factor 4.3 in accordance with the measurement of [30]. The hadronisation step proceeds according to the Lund string model for light quarks and the Peterson model for heavy quarks. The simulation is adjusted to reproduce the world average results on the relative abundances of charmed mesons [31]. The generated events are then processed by the H1 detector simulation program and are subjected to the same reconstruction and analysis chain as the real data.

2.2 Selection of DIS Events

The analysis is based on events which contain a scattered positron detected in the SpaCal backward calorimeter. Scattered positrons are identified as clusters in the SpaCal with energies $E_{e'} > 8$ GeV, with cluster radii less than 3.5 cm, consistent with an electromagnetic energy deposition. The cluster centres must be spatially associated with a charged track candidate in the BDC within the polar angular region $153^\circ < \theta < 177.8^\circ$. The events are triggered by the identification of a SpaCal cluster in coincidence with a central charged track signal from the MWPC and central drift chamber triggers.

At fixed $\sqrt{s}$ the kinematics of the scattering process are determined by two of the Lorentz invariant variables Q^2, y and the Bjorken scaling variable x. These variables are reconstructed using the scattered positron according to

$$Q^2 = 4E_e E_{e'} \cos^2\left(\frac{\theta_{e'}}{2}\right), \quad y = 1 - \frac{E_{e'}}{E_e}\sin^2\left(\frac{\theta_{e'}}{2}\right), \qquad x = \frac{Q^2}{ys}, \tag{3}$$

with E_e and $E_{e'}$ denoting the energies of the incoming and scattered positron, respectively, and $\theta_{e'}$ the polar angle of the scattered positron.

2.3 Decay Vertex Reconstruction

The lifetimes of between 0.4 and 1 ps of the D mesons lead to a spatial separation between their production vertex, assumed to be the point of the primary ep interaction, and the decay vertex, referred to as the secondary vertex. This separation is expressed here in terms of the radial decay length l and its error σ_l. The decay length measures the distance between these two vertices in the r-ϕ plane, which is typically a few hundred μm. The significance $S_l = l/\sigma_l$ is a powerful discriminator to identify long-lived hadrons [32].

Tracks are first reconstructed in the CJC and are then extrapolated into the CST, where the closest hit from strips measuring r-ϕ in each layer is associated with each track if it lies within 5σ of the extrapolated CJC track. Then the tracks are refitted using the additional information of the CST hits. Two or three such CST-improved tracks are used to form a D meson candidate by fitting them to a common secondary vertex in the r-ϕ plane, while all other tracks in the event, CST-improved or not, are used for the determination of the primary vertex.

For the primary vertex fit an iterative procedure is adopted. The track with the largest contribution to the χ^2 is removed and the fit is repeated until the χ^2 contribution of each track assigned to the primary vertex is less than three. The precisely known position and profile of the elliptical interaction region in the r-ϕ plane ("beam spot") enter the primary vertex fit as an additional measurement of the vertex coordinates with uncertainties given by the width of the interaction region.

The position of the beam spot is determined run-wise or for a large number of events inside a run by averaging the reconstructed ep interaction points. The profile of the beam spot is assumed to be Gaussian and stable throughout the data-taking period. Its width is determined from a sample of events where the primary vertex is accurately measured from high momentum central tracks, which are largely unaffected by multiple scattering. Widths of 145 μm and 25 μm are found for the horizontal and vertical directions, respectively. The uncertainty of the primary vertex determination varies from event to event with an average 69 μm in the horizontal direction. The uncertainty in the vertical direction is essentially given by the 25 μm vertical width of the beam spot.

In the fit for the secondary vertex the momentum of the D meson candidate is constrained to be parallel (or anti-parallel) to the vector connecting the primary and secondary vertices. This provides a powerful constraint to reject random track combinations. The primary vertex position and its error are used as external measurements in the fit. The uncertainty on the decay length is dominated by the resolution of the secondary vertex reconstruction.

D meson decay candidates are selected by applying requirements on the following variables: the minimal transverse momentum p_t of daughter tracks, a signed impact parameter[3] d of significance $S_d = d/\sigma_d$ for at least two tracks, the secondary vertex fit probability $\mathcal{P}_{VF}$, the error on the decay length measurement σ_l and the vertex separation significance $S_l = l/\sigma_l$. The detailed cuts, chosen to optimise the signal significance, are listed in table 1. At most one missing CST hit is allowed for each D meson candidate. The CST geometry confines the D mesons to lie in a polar angular range of typically $25^\circ < \theta < 155^\circ$.

To test the understanding of the CST, its response to data has been compared with simulations for a sample of "tagged" D^0 mesons (figure 2a). These D^0 mesons originate from a $D^{*+} \to D^0\pi_s^+ \to (K^-\pi^+)\pi_s^+$ decay chain and are selected by a cut about the nominal value of $\Delta m = m(K\pi\pi_s) - m(K\pi)$ corresponding to a window of three times the resolution. In this channel a good signal purity can be achieved without a lifetime cut, thus allowing a determination of the efficiency of the CST reconstruction. Figure 2b shows the measured decay length significance distribution S_l of tagged D^0 candidates, together with its fitted decomposition into

[3]The impact parameter d is the distance of closest approach of a track to the primary vertex. It is positive if the angle between the momentum vector of the D meson candidate and the vector pointing from the primary vertex to the point of closest approach is less than 90°.

a signal and a background contribution. The functional form of the signal distribution is taken from the simulation, whereas the background shape is extracted from the sideband regions on both sides of the nominal D^0 mass in the $m(K\pi)$ spectrum of the data, as indicated in figure 2a. In the fit of the S_l distribution only the normalisations of the signal and of the background are left as free parameters. The $\chi^2/ndf = 34/32$ indicates that the MC simulation describes the signal shape very well. Furthermore, the number of D^0 candidates extracted by means of the S_l fit is found to be fully consistent with the number determined from the fit shown in figure 2a) to the invariant mass distribution $m(K\pi)$.

To illustrate the purity that can be reached, the invariant mass distributions for $D^+ \to K^+\pi^-\pi^+$ candidate events are compared before and after a stringent cut $S_l > 8$ in figure 3. The signal-to-background ratio improves by a factor 50 while 20% of the signal is retained. For the cross section measurements described below a less stringent cut $S_l > 5$ is chosen to increase the efficiency, albeit with a reduced purity.

2.4 Signal Determination

The reconstruction of D mesons uses all CST-improved charged particle tracks. No explicit particle identification is applied, and each track is assumed to be either a kaon or a pion as appropriate. The tracks of suitable charge are required to pass the transverse momentum criteria specified in table 1. They are then fitted to a common secondary vertex, which must also fulfil the requirements listed in table 1. The number of signal events is then determined for each D meson individually by fitting the invariant mass distributions of the candidate combinations with a Gaussian to describe the signal and an appropriate background shape. The signal mass and width are left free in the fit. The invariant mass distributions used to extract the final number of signal events after all the vertexing cuts are shown in figure 4. The specific choices for the fits are the following:

a) $D^+ \to K^-\pi^+\pi^+$: the 3-particle invariant mass distribution $m(K\pi\pi)$ is fitted using a Gaussian for the signal and a linear function describing the background shape (figure 4a).

b) $D^0 \to K^-\pi^+$: the 2-particle invariant mass distribution $m(K\pi)$ (figure 4b) is fitted using a Gaussian for the signal, an exponentially falling function to describe the combinatorial background and a contribution from wrong-charge combinations. The latter contribution arises since with no particle identification applied, each $D^0 \to K^-\pi^+$ decay also enters the distribution as a $\bar{D^0} \to K^+\pi^-$ candidate. The contribution of this wrong-charge assignment is modelled by a broad Gaussian with the mean position, the width and the normalisation relative to the correct-charge Gaussian determined from the simulation and subsequently kept fixed in the fit.

c) $D_s^+ \to \phi\pi^+ \to (K^+K^-)\pi^+$: because the D_s decays via the intermediate vector meson resonance ϕ, it has a restricted 3-body phase space, allowing criteria to be applied to suppress the combinatorial background. In particular, the 2-particle combination $m(K^+K^-)$ is required to lie within a $\pm 2\sigma$ window (± 11 MeV) around the nominal ϕ mass. The distribution in the cosine of the angle θ^* (helicity angle), defined as the angle between the K-momentum vector and the D_s flight direction, transformed into the ϕ rest frame, follows a $\cos^2\theta^*$ shape. A value of $|\cos\theta^*| > 0.4$ is required. The 3-particle invariant mass distribution $m(KK\pi)$, fitted using a Gaussian for the signal and an exponential background function, is shown in figure 4c.

d) $D^{*+} \to D^0\pi_s^+ \to (K^-\pi^+)\pi_s^+$: the Δm-tagging technique is applied [33]. For all candidate combinations lying within a 3 sigma window ($\pm$ 3.6 MeV) of the nominal value of $\Delta m = m(K\pi\pi_s) - m(K\pi)$, the invariant mass distribution $m(K\pi)$ is fitted using a Gaussian for the signal and an exponential function describing the background shape. The Figure 4d shows this $m(K\pi)$ distribution after the cut on Δm.

The fitted D meson mass values are all found to be compatible within errors with the world average values [34], and the widths are in agreement with the expected detector resolutions. For the D meson differential distributions the data sample is divided into bins and the number of signal events is extracted in each bin separately. The position and width of the Gaussian describing the signal are fixed to the values found in the inclusive sample. If left free both positions and widths are found to be stable.

2.5 Acceptance and Efficiency Determination

The Monte Carlo simulation of charm and beauty production is used to determine the detector acceptance and the efficiency of the reconstruction and selection cuts. The detector efficiencies are determined to be around 60% for events within the combined geometric and kinematic acceptances, which vary between 36% and 62% for the different mesons. The lifetime tagging efficiencies are found to be 19%, 11%, 21% and 39%, for D^+, D^0, D_s^+ and D^{*+}, respectively. Migrations due to the limited detector resolution are small for the chosen bin sizes in the differential distributions and are corrected by means of Monte Carlo simulation.

2.6 Cross Section Determination and Systematic Errors

The visible cross section σ_{vis} is defined for the sum of the observed number of D mesons, N_D, for both particle and antiparticle meson states according to the formula

$$\sigma_{vis}(ep \to e'DX) = \frac{N_D + N_{\bar{D}}}{\mathcal{L} \cdot \epsilon \cdot (1 + \delta_{rad})} \quad , \tag{4}$$

where $\mathcal{L}$ denotes the integrated luminosity and ϵ the total efficiency including all acceptances and branching ratios, which are taken from [34]. The radiative corrections δ_{rad} correct the measured cross sections to the Born level and are calculated using the program HECTOR [35]. They amount to $\delta_{rad} = 2.6\%$ on average and vary between -4% and $+9\%$ over the kinematic range considered.

The systematic errors on σ_{vis}, summarised in table 2, are dominated by the uncertainty on the CJC tracking efficiency (conservatively estimated to $^{+5}_{-1}\%$ per track in this analysis). A 10% uncertainty is assigned to the lifetime cut efficiency to account for a possible inaccuracy in the description of the resolution function in the simulation. This number is estimated by variations of the S_l-cut and covers the differences between data and simulation [32]. The CST efficiency uncertainty is 1% per hit.

The systematic error on the signal extraction is determined by variation of the background shapes in the fits. Backgrounds to the signals from other charm decays are estimated from

Monte Carlo simulations to be at most 3% and are also included in the systematic errors. The dependence of the simulated acceptances and effi ciencies on parameter choices made for the simulation (charm mass, parton density distributions, fragmentation parameters and QCD scales, cf. section 2.7) is found to be less than $\pm 2\%$ in all cases and is included in the systematic error.

The uncertainty on the absolute SpaCal electromagnetic energy scale contributes a maximal change in σ_{vis} of $^{+4}_{-9}\%$. The error due to initial state radiation (ISR) corrections is estimated to be $\pm 2.6\%$, the average size of the correction itself. The results obtained when reconstructing the kinematic variables using the scattered positron have been checked with the Σ-method, which combines the hadronic fi nal state and the positron measurement [36] and are found to be in good agreement.

The electron detection, the tracking and the vertexing errors are to a large extent common between the different mesons and result in correlated systematic errors of about 15%. The D_s meson suffers from a particularly large (24.7%) uncertainty due to the poorly known branching fraction to $\phi\pi$.

2.7 Theoretical predictions and uncertainties

The measured cross sections are compared with LO QCD predictions based on the AROMA 2.2 [28] program, which incorporates the universality ansatz. The predictions include the contributions from decays of excited charmed hadrons. For the nominal predictions the program is run using the GRV-98 proton structure function parametrisation [37], a charm quark mass of $m_c = 1.5$ GeV and Peterson fragmentation with $\epsilon_c = 0.078$. The contributions of decays of beauty hadrons is simulated using a quark mass of $m_b = 4.75$ GeV and $\epsilon_b = 0.0069$. It is scaled to reproduce the result of [30]. The renormalisation and factorisation scales are both set to $\mu = \sqrt{Q^2 + m_t^2(q) + m_t^2(\bar{q})}$, where $m_t(q) = \sqrt{p_t^2 + m_q^2}$ is the "transverse" mass of the quark q. The prediction uncertainties are estimated by simultanously changing the renormalisation and factorisation scales by a factor of two or 0.5, varying m_c between 1.4 GeV and 1.6 GeV, and changing ϵ_c to 0.048. The contributions are added in quadrature. They are dominated by the quark mass and fragmentation parameter variations (for details see [32]).

For the D^* meson production cross section the AROMA prediction is also compared with a next to leading order (NLO) calculation in the DGLAP scheme [38] using the HVQDIS program [39]. The GRV98-HO parton densities of the proton [37] are used, supplemented by a Peterson fragmentation parametrisation with $\epsilon_c = 0.035$ and $\epsilon_b = 0.0033$ as in [12, 40]. The renormalisation and factorisation scales are both set to $\mu = \sqrt{Q^2 + 4m_q^2}$ with the same quark mass values as are used for the AROMA simulation. The uncertainties on the NLO prediction are estimated analogously to the LO case. They are dominated by variations of the renormalisation and factorisation scales and by changing the mass m_c between 1.3 GeV and 1.7 GeV [11]. Added in quadrature, the total uncertainties are of approximately 15%.

3 Results

3.1 Differential Production Cross Sections

Differential production cross sections are determined for all four D mesons individually and are tabulated in tables 6-9. As an example the results for the D^+ meson are shown in figure 5 as a function of the kinematic variables $p_t(D^+)$, $\eta(D^+)$, Q^2 and y. For all mesons the cross sections fall rapidly with Q^2 and $p_t(D)$, as expected from the hard scattering. The distributions are well reproduced by the LO AROMA simulation, which is overlaid in figure 5. The estimated beauty contributions are shown separately as dashed lines. The shaded bands indicate the uncertainties on the predictions. The differential distributions for the remaining D^0, D_S and D^* mesons are equally well described by the LO QCD simulation [32].

For a direct comparison of the differential cross sections extracted for the four different D mesons, the differential cross sections have been scaled with the inverse fragmentation factors derived further below (cf. table 4) and are shown in figure 6 as a function of $p_t(D)$, $\eta(D)$ and Q^2. Within the present experimental accuracy the normalised cross sections are compatible with one another.

3.2 Inclusive Production Cross Sections

The inclusive electroproduction cross sections are determined in the visible kinematic range of $2 \leq Q^2 \leq 100$ GeV^2, $0.05 \leq y \leq 0.7$, $p_t(D) \geq 2.5$ GeV and $|\eta(D)| \leq 1.5$. The measured values for the four D mesons are summarised in table 3.

The D^* meson results are consistent with earlier measurements at HERA [2–5, 41] once the differences in kinematic regions are taken into account. For the D^* meson the visible production cross section has also been calculated in the next to leading order (NLO) DGLAP scheme [38] with the HVQDIS program [39] (see section 2.7). The NLO prediction yields a value of $\sigma_{vis} = 2.76 \pm 0.41$ nb for the D^*, which is in good agreement with the LO AROMA value of 2.61 ± 0.31 nb.

3.3 Fragmentation Factors and Ratios

In the absence of decays of excited intermediate charm states, the relative abundance of the various charmed hadrons is given by the primary production rate, which is directly proportional to n_D, the normalisation of the fragmentation functions (equation 2). However, the experimentally determined fragmentation factors $f(c \to D)$ include all possible decay chains that result in that particular D meson, in addition to the direct production. Thus, the measured pseudoscalar D^+, D^0 and D_s mesons contain a large fraction of mesons produced in $D^*_{(s)}$ decays.

The fragmentation factors $f(c \to D)$ are deduced from a comparison of the measured cross sections σ_{vis} with the LO expectation σ^{MC}_{vis} after correcting for the beauty contribution to which an uncertainty of 50% is attributed. Explicitly, the following relationship is used:

$$f(c \to D) = \frac{\sigma_{vis}(ep \to e'DX) - \sigma_{vis}^{MC}(ep \to e'b\bar{b}X' \to e'DX)}{\sigma_{vis}^{MC}(ep \to c\bar{c} \to e'DX)} \cdot f_{\mathrm{wa}}(c \to D). \quad (5)$$

The resulting values for $f(c \to D)$ are listed in table 4. For comparison, the world average values $f_{\mathrm{wa}}(c \to D)$ are also shown. The measurements $f(c \to D)$ agree well within errors with the world average values $f_{\mathrm{wa}}(c \to D)$.

Constraints can be explicitly imposed on the measurements to improve the experimental accuracy. The constraint

$$1 \;=\; f(c \to D^+) + f(c \to D^0) + f(c \to D_s) + f(c \to \Lambda_c, \Xi_c, \Omega_c) \quad (6)$$

introduces contributions of fragmentation to charmed baryons, which are not determined in this analysis. World average values [34] are taken instead, yielding a total of $f(c \to \Lambda_c, \Xi_c, \Omega_c) = 8.64 \pm 2.50\%$.

The constraint

$$f(c \to D^+) \;=\; f(c \to D^0) - 2 \cdot f(c \to D^{*+}) \cdot \mathcal{B}(D^{*+} \to D^0\pi) \quad (7)$$

is derived by assuming isospin symmetry independently in both the vector and pseudoscalar sectors ($n_{D^{*+}} = n_{D^{*0}}$ and $n_{D^+} = n_{D^0}$). The branching fraction $\mathcal{B}(D^{*+} \to D^0\pi)$ is taken as 67.6 ± 0.5 % [34]. The D^{*0} mesons, which are not explicitly reconstructed in this analysis, are assumed to decay entirely into final states containing a D^0 meson [34].

The results of a fit for the fragmentation factors using the constraints of equation 6 and equation 7 are listed separately in table 4 as $f_{\mathrm{constraint}}(c \to D)$. The fit takes the correlations of the uncertainties between the different mesons into account. In comparison with the unconstrained results the errors are reduced and the value $f(c \to D^0)$ moves closer to the world average, whereas the other factors do not change significantly.

Ratios of fragmentation factors are useful to characterise distinct aspects of fragmentation, such as the proportions of light quark flavours u, d and s created in the fragmentation process and the formation of different angular momentum states. Such quantities have been measured in light quark fragmentation and charm fragmentation in e^+e^- annihilation [12, 18–20]. It is important to verify their applicability for deep inelastic scattering.

Various ratios are extracted from the D meson fragmentation factors obtained without the constraints of equations 6 and 7. The common experimental uncertainties largely cancel in this procedure. Expressed both in terms of the normalisation factors for primary D mesons produced, n_D, and in terms of the experimentally accessible fragmentation factors $f(c \to D)$, the ratios considered are:

$$P_V^d = \frac{n_{D^{*+}}}{n_{D^{*+}} + n_{D^+}} = \frac{f(c \to D^{*+})}{f(c \to D^+) + f(c \to D^{*+}) \cdot \mathcal{B}(D^{*+} \to D^0\pi^+)}; \quad (8)$$

$$P_V^{u+d} = \frac{2 \cdot n_{D^{*+}}}{n_{D^{*+}} + n_{D^+} + n_{D^{*0}} + n_{D^0}} = \frac{2 \cdot f(c \to D^{*+})}{f(c \to D^+) + f(c \to D^0)}; \quad (9)$$

$$R_{u/d} = \frac{n_{D^{*0}} + n_{D^0}}{n_{D^{*+}} + n_{D^+}} = \frac{f(c \to D^0) - f(c \to D^{*+}) \cdot \mathcal{B}(D^{*+} \to D^0\pi^+)}{f(c \to D^+) + f(c \to D^{*+}) \cdot \mathcal{B}(D^{*+} \to D^0\pi^+)}; \quad (10)$$

$$\gamma_s = \frac{2 \cdot (n_{D_s^{*+}} + n_{D_s^+})}{n_{D^{*+}} + n_{D^+} + n_{D^{*0}} + n_{D^0}} = \frac{2 \cdot f(c \to D_s^+)}{f(c \to D^+) + f(c \to D^0)}. \quad (11)$$

The fragmentation characteristics derived according to equations 8-11 are summarised in table 5. The ratio P_V measures the fraction of vector mesons produced in the fragmentation chain. This ratio has been evaluated separately for the $c\bar{d}$-quark combination (equation 8) and the sum of $c\bar{u}$ and $c\bar{d}$ quark combinations (equation 9). Isospin invariance $f(c \to D^{*+}) = f(c \to D^{*0})$ has been assumed for P_V^{u+d} and the result agrees well with values measured at LEP [42, 43]. The P_V^d result is larger than the LEP value by around 1.5 sigma.

The ratio $R_{u/d}$ of probabilities for a charm quark to hadronise together with a u or d-quark agrees well with a value of unity, as is also the case at LEP [42]. The suppression of s-quarks with respect to u and d quarks is measured by the factor γ_s. The value of γ_s extracted in this analysis suggests a suppression of almost a factor 3. This observation agrees well with the suppression factor measured in the fragmentation of primary light quarks and with measurements of charm fragmentation in e^+e^- [44].

4 Conclusions

Production cross sections of the charmed mesons D^+, D^0, D_s and D^{*+} are measured in deep inelastic ep collisions at HERA. The measurements rely on the precise reconstruction of the D meson production and decay vertices using the central silicon tracker of the H1 detector. The differential production cross sections of all four D mesons measured in the same kinematic region show a very similar dependence on the transverse momentum $p_t(D)$ and the pseudorapidity $\eta(D)$ of the charmed hadron, as well as on the photon virtuality Q^2.

Based on the measured cross sections, the fragmentation factors $f(c \to D)$ are extracted. They are found to agree with the world average values, which are dominated by measurements made in e^+e^- collisions. Based on ratios of these $f(c \to D)$ the fragmentation-sensitive parameters P_V, $R_{u/d}$ and γ_s are determined. They are also in agreement with the world average values.

The measurements of the cross sections and of the fragmentation-sensitive ratios thus support the validity of the commonly made assumptions that the charm quark production and the fragmentation processes factorise and that the non-perturbative component of the hadronisation $D_D^{(c)}(z)$ is well described by a universal fragmentation ansatz, independent of the hard scattering process and of the charm production scale.

Acknowledgements

We are grateful to the HERA machine group whose outstanding efforts have made this experiment possible. We thank the engineers and technicians for their work in constructing and maintaining the H1 detector, our funding agencies for financial support, the DESY technical staff for continual assistance and the DESY directorate for support and for the hospitality which they extend to the non DESY members of the collaboration.

References

[1] S. Aid *et al.* [H1 Collaboration], Nucl. Phys. B **472** (1996) 32 [arXiv:hep-ex/9604005].

[2] C. Adloff *et al.* [H1 Collaboration], Nucl. Phys. B **545** (1999) 21 [arXiv:hep-ex/9812023].

[3] C. Adloff *et al.* [H1 Collaboration], Phys. Lett. B **528** (2002) 199 [arXiv:hep-ex/0108039].

[4] J. Breitweg *et al.* [ZEUS Collaboration], Eur. Phys. J. C **12** (2000) 35 [arXiv:hep-ex/9908012].

[5] S. Chekanov *et al.* [ZEUS Collaboration], Phys. Rev. D **69** (2004) 012004 [arXiv:hep-ex/0308068].

[6] R. K. Ellis and P. Nason, Nucl. Phys. B **312** (1989) 551.

[7] J. Smith and W. L. van Neerven, Nucl. Phys. B **374** (1992) 36.

[8] E. Laenen, S. Riemersma, J. Smith and W. L. van Neerven, Nucl. Phys. B **392** (1993) 162; and *ibid* B **392** (1993) 229.

[9] S. Frixione, M. L. Mangano, P. Nason and G. Ridolfi , Nucl. Phys. B **412** (1994) 225 [arXiv:hep-ph/9306337].

[10] S. Frixione, M. L. Mangano, P. Nason and G. Ridolfi , Nucl. Phys. B **431** (1994) 453.

[11] S. Frixione *et al.*, J. Phys. G **27** (2001) 1111.

[12] P. Nason and C. Oleari, Nucl. Phys. B **565** (2000) 245 [arXiv:hep-ph/9903541].

[13] J. C. Collins, Phys. Rev. D **58** (1998) 094002 [arXiv:hep-ph/9806259].

[14] B. Mele and P. Nason, Nucl. Phys. B **361** (1991) 626.

[15] P. Nason and B. R. Webber, Nucl. Phys. B **421** (1994) 473 and erratum *ibid* B **480** (1996) 755.

[16] P. Nason *et al.*, in LHC workshop on Standard Model Physics, "Bottom production", arXiv:hep-ph/0003142.

[17] C. Peterson, D. Schlatter, I. Schmitt and P. M. Zerwas, Phys. Rev. D **27** (1983) 105.

[18] H. Albrecht *et al.* [ARGUS Collaboration], Z. Phys. C **52** (1991) 353.

[19] R. Akers *et al.* [OPAL Collaboration], Z. Phys. C **67** (1995) 27.

[20] D. Buskulic *et al.* [ALEPH Collaboration], Phys. Lett. B **357** (1995) 699.

[21] I. Abt *et al.* [H1 Collaboration], Nucl. Instrum. Meth. A **386** (1997) 310 and *ibid* 348.

[22] J. Bürger *et al.*, Nucl. Instrum. Meth. A **279** (1989) 217.

[23] I. Abt *et al.* [H1 Collaboration], Phys. Lett. B **328** (1994) 176.

[24] D. Pitzl *et al.*, Nucl. Instrum. Meth. A **454** (2000) 334 [arXiv:hep-ex/0002044].

[25] K. Müller *et al.*, Nucl. Instrum. Meth. A **312** (1992) 457.

[26] R. D. Appuhn *et al.* [H1 SPACAL Group Collaboration], Nucl. Instrum. Meth. A **386** (1997) 397.

[27] H1 Collaboration, Technical proposal for the upgrade of the backward region of the H1 detector, Hamburg DESY - PRC 93-02.

[28] G. Ingelman, J. Rathsman and G. A. Schuler, Comput. Phys. Commun. **101** (1997) 135 [arXiv:hep-ph/9605285].

[29] T. Sjöstrand, Comput. Phys. Commun. **82** (1994) 74.

[30] T. Sloan [H1 Collaboration], "Heavy flavor production at HERA," 36th Rencontres de Moriond, France, Mar 2001, arXiv:hep-ex/0105064;
F. Sefkow [H1 Collaboration], "Heavy quark production in deep-inelastic scattering," Int. EPS Conf. on High Energy Physics, July 2001, Budapest, Hungary, arXiv:hep-ex/0110036.

[31] L. Gladilin, arXiv:hep-ex/9912064.

[32] J. Gassner, Dissertation, DISS-ETH-14774, Zürich, 2002, unpublished, also available at http://www-h1.desy.de/publications/theses_list.html.

[33] G. J. Feldman *et al.*, Phys. Rev. Lett. **38** (1977) 1313.

[34] D. E. Groom *et al.* [Particle Data Group Collaboration], Eur. Phys. J. C **15** (2000) 1.

[35] A. Arbuzov *et al.*, Comput. Phys. Commun. **94**, 128 (1996) [arXiv:hep-ph/9511434].

[36] U. Bassler and G. Bernardi, Nucl. Instrum. Meth. A **361** (1995) 197 [arXiv:hep-ex/9412004].

[37] M. Glück, E. Reya and A. Vogt, Eur. Phys. J. C **5** (1998) 461 [arXiv:hep-ph/9806404].

[38] V. N. Gribov and L. N. Lipatov, Yad. Fiz. **15**, 781 (1972) [Sov. J. Nucl. Phys. **15**, 438 (1972)];
V. N. Gribov and L. N. Lipatov, Yad. Fiz. **15**, 1218 (1972) [Sov. J. Nucl. Phys. **15**, 675 (1972)];
L. N. Lipatov, Sov. J. Nucl. Phys. **20**, 94 (1975), [Yad. Fiz. **20**, 181 (1974)];
G. Altarelli and G. Parisi, Nucl. Phys. B **126**, 298 (1977) ;
Y. L. Dokshitzer, Zh. Eksp. Teor. Fiz. **73**, 1216 (1977), [Sov. Phys. JETP **46**, 641 (1977)].

[39] B. W. Harris and J. Smith, Phys. Rev. D **57** (1998) 2806 [arXiv:hep-ph/9706334].

[40] P. Nason and C. Oleari, Phys. Lett. B **447** (1999) 327 [arXiv:hep-ph/9811206].

[41] C. Adloff *et al.* [H1 Collaboration], Phys. Lett. B **520** (2001) 191 [arXiv:hep-ex/0108047].

[42] R. Barate *et al.* [ALEPH Collaboration], Eur. Phys. J. C **16** (2000) 597 [arXiv:hep-ex/9909032].

[43] P. Abreu *et al.* [DELPHI Collaboration], Eur. Phys. J. C **12** (2000) 225.

[44] G. Altarelli *et al.*, *Workshop on Physics at LEP2*, CERN Report CERN-96-01-V-2 (1996) p.112.

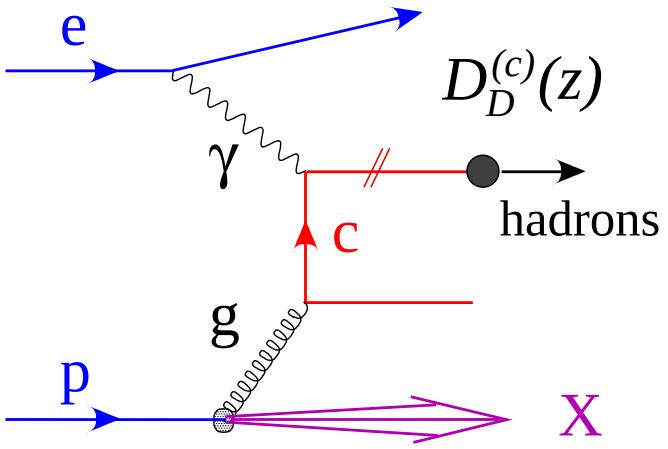

Figure 1: *Diagram for the production of c-quarks in ep collisions via the photon-gluon fusion process. The hadronisation into a charmed meson D is described by the fragmentation function $D_D^{(c)}(z)$ (cf. equation 2).*

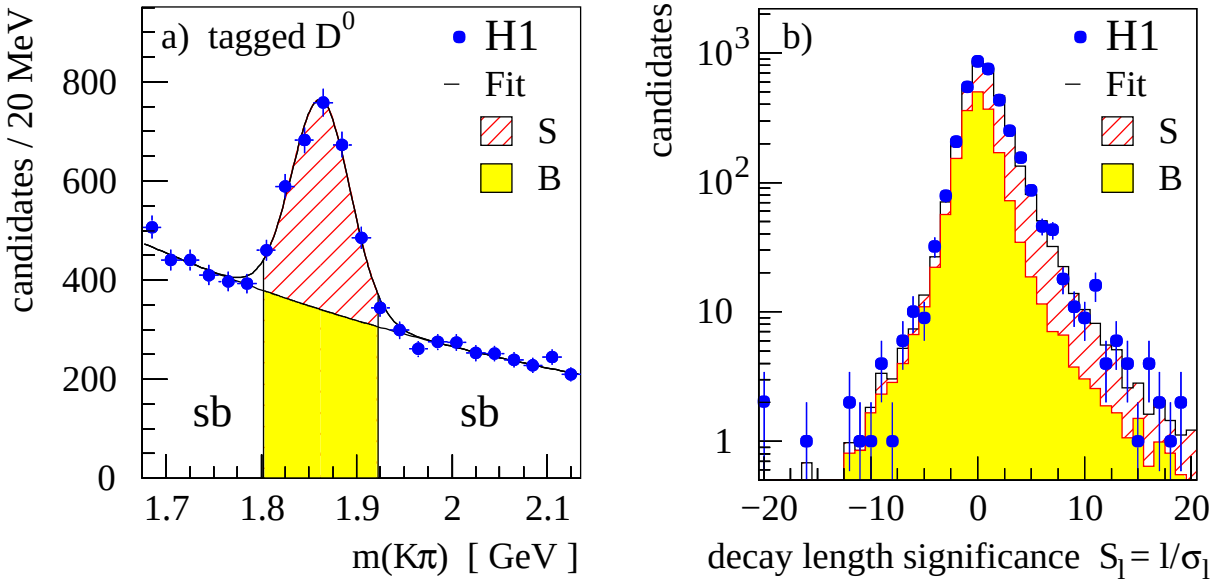

Figure 2: *a) Invariant mass distribution $m(K\pi)$ and b) signed decay length significance distribution S_l measured for tagged D^0 mesons in data (solid points). Superimposed is the fitted decomposition into signal (S, hatched) and background (B, shaded) contributions (see text). The background in b) is determined from the $m(K\pi)$ sideband regions (sb) as indicated in a).*

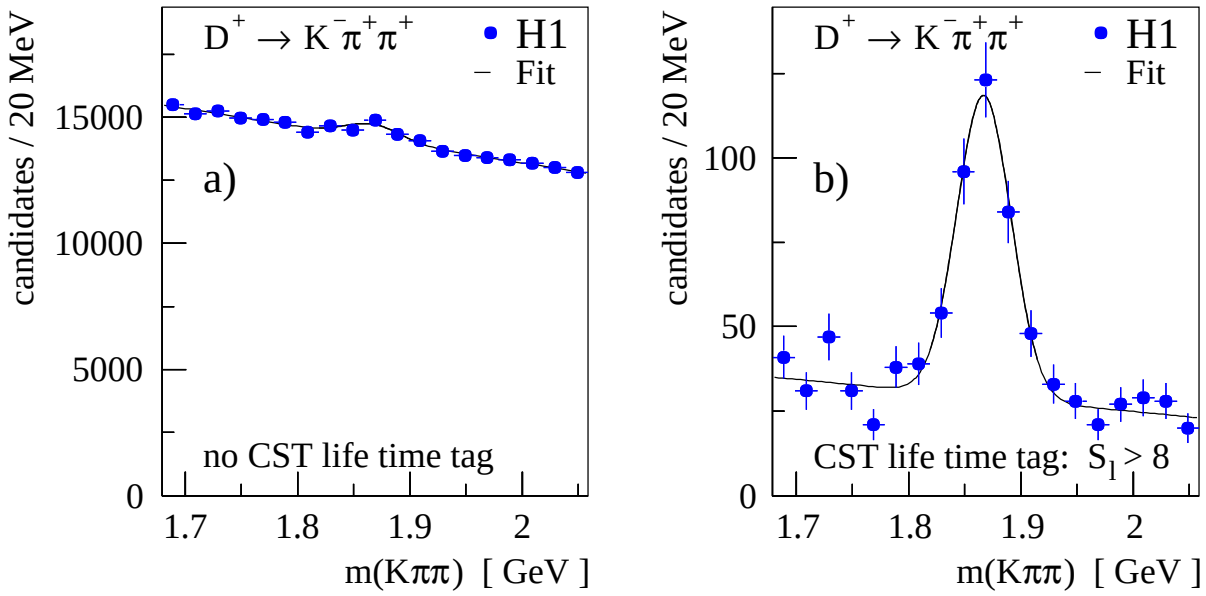

Figure 3: *Invariant mass distributions* $m(K\pi\pi)$ *for* $D^+ \to K^-\pi^+\pi^+$ *decay candidates (a) before and (b) after a cut on the decay length significance* $S_l > 8$.

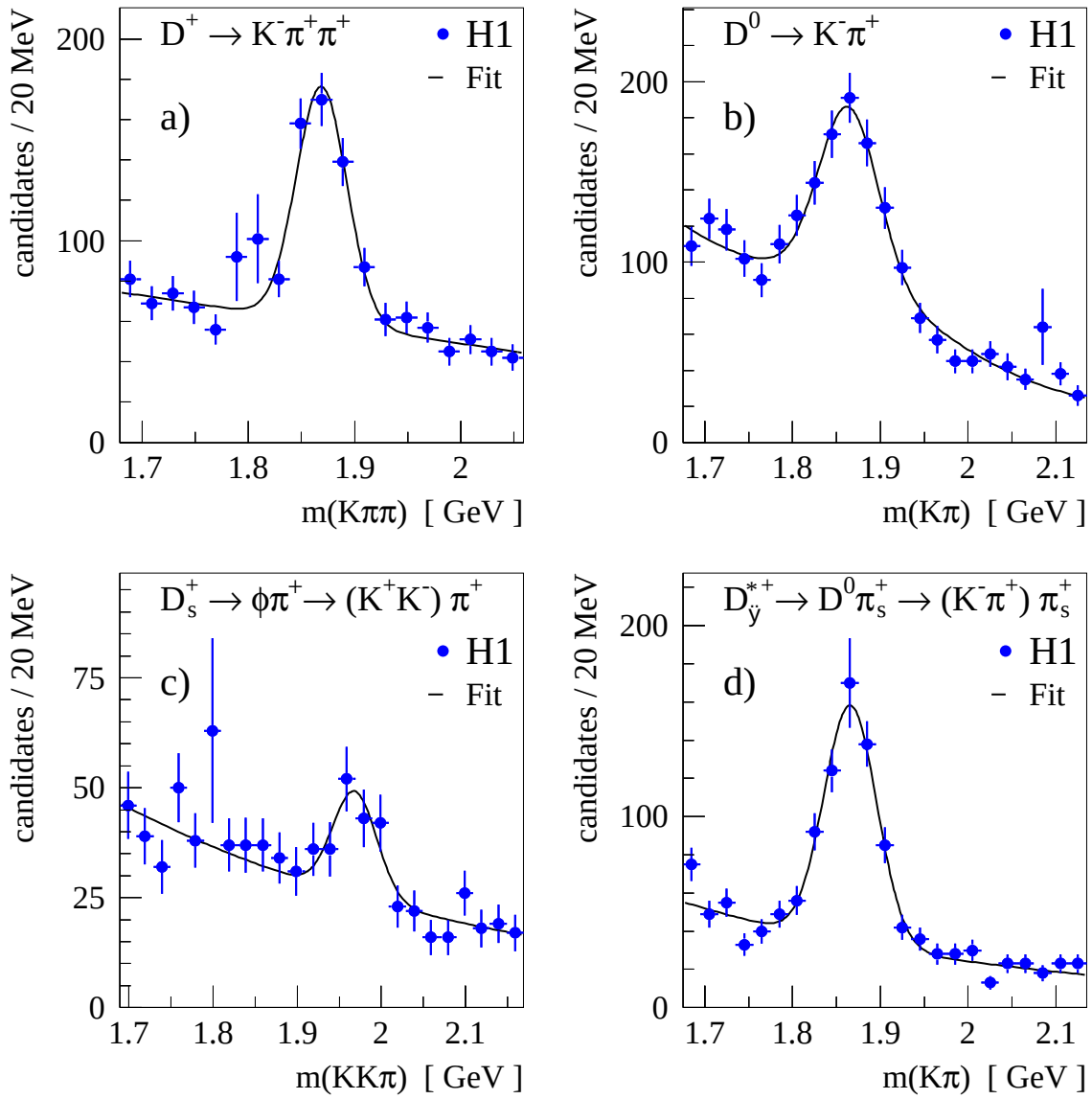

Figure 4: *Invariant mass distributions for the four D meson candidate decays that are used to determine the number of signal events: a) $D^+ \to K^-\pi^+\pi^+$, b) $D^0 \to K^-\pi^+$, c) $D_s^+ \to \phi\pi^+ \to K^+K^-\pi^+$ and d) $D^{*+} \to D^0\pi_s^+ \to K^-\pi^+\pi_s^+$ (the invariant mass $m(K\pi)$ is shown after the Δm cut). The curves show the fits in which the signals are described by a Gaussian and the backgrounds are parametrised as discussed in the text.*

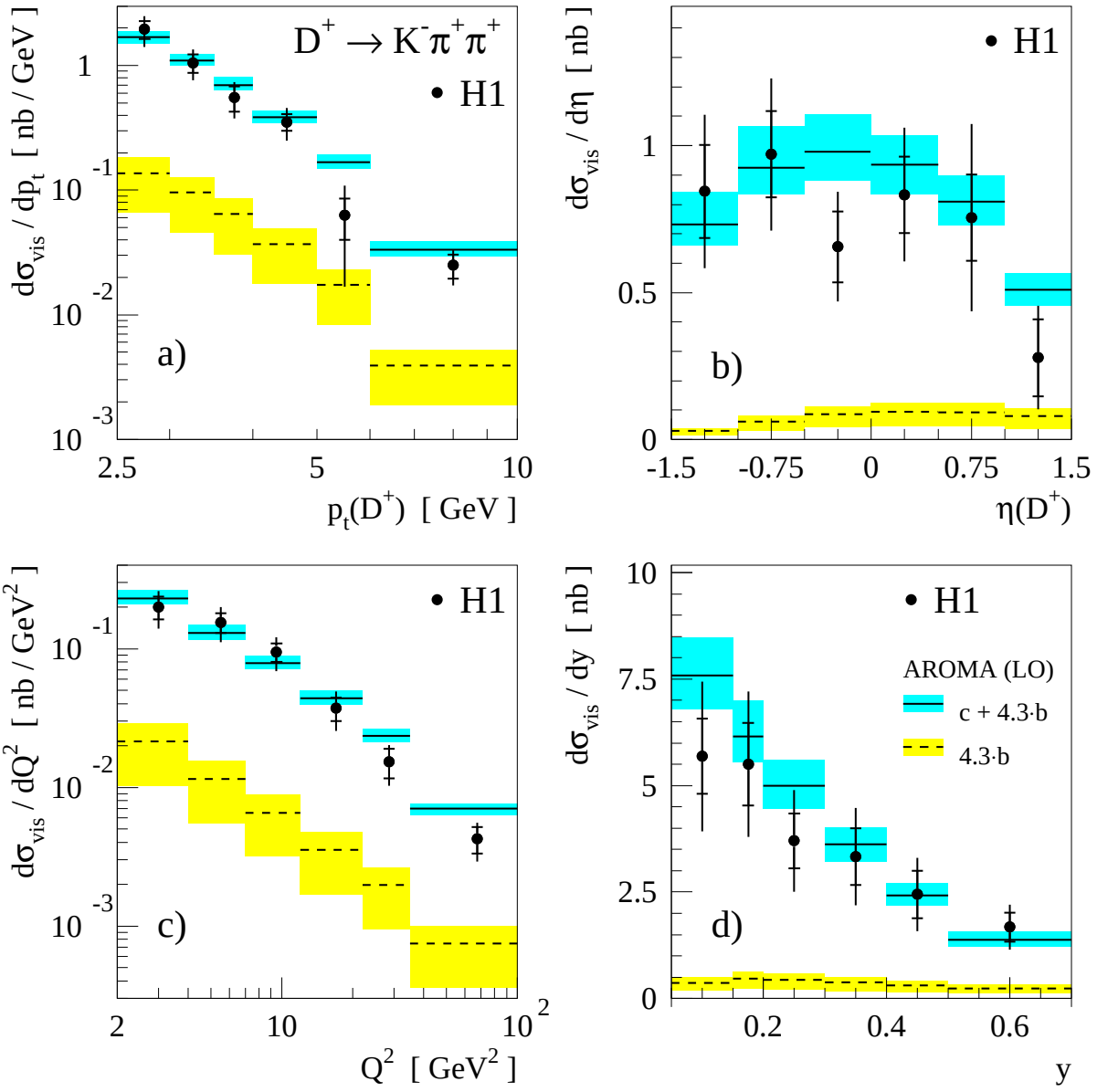

Figure 5: *Differential production cross section for D^+ as a function of a) the D^+ transverse momentum $p_t(D^+)$, b) the pseudorapidity $\eta(D^+)$, c) the photon virtuality Q^2, and d) the inelasticity y. The symbols denote the values averaged over the bins and are plotted at the bin centres. The error bars show the statistical (inner bars) and the total (outer bars) errors, respectively. The solid lines show the LO AROMA predictions including scaled beauty contributions, shown separately as dashed lines. The shaded bands indicate the uncertainties on the predictions (see text).*

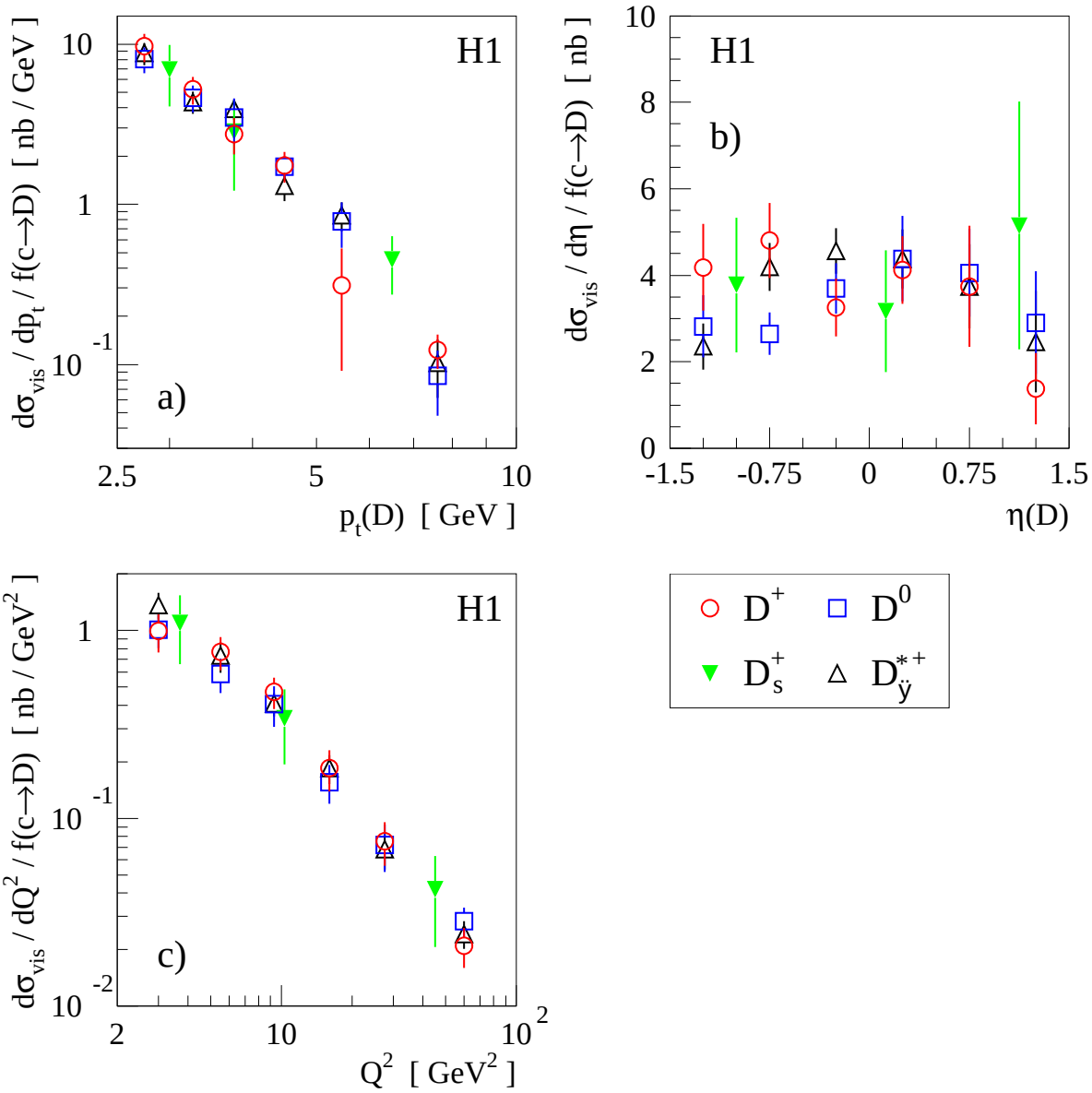

Figure 6: *Visible differential production cross sections for all four D mesons, divided by their respective measured fragmentation factors, are shown as a function of a) the D meson transverse momentum $p_t(D)$, b) the pseudorapidity $\eta(D)$, and c) photon virtuality Q^2. The error bars indicate the quadratic sum of the statistical errors and the systematic errors which are not common to the different D mesons. An overall common systematic error of 15% is not shown. The cross sections are displayed on the horizontal axis at the position that corresponds to the average differential cross section, obtained using the AROMA simulation.*

Selection criteria	D^+	D^0	D_s^+	D^{*+}
min $p_t(K)$ [MeV]	500	800	400	250
min $p_t(\pi)$ [MeV]	400	800	400	250
min $p_t(\pi_s)$ [MeV]	-	-	-	140
min impact par. sig. S_d	2.5	2	1	-1
min decay length sig. S_l	5	3	2	1
max decay length error σ_l	300 μm			
min fit probability $\mathcal{P}_{VF}$	0.05			

Table 1: *Selection criteria for each of the four D mesons. Listed are the minimal transverse momenta of the daughter tracks (cuts on the slow pion π_s are only applicable for the D^* meson) and the requirements on the vertexing parameters (see text).*

Source of uncertainty	D^+	D^0	D_s^+	D^{*+}
CJC efficiency	$^{+15.0}_{-3.0}$	$^{+10.0}_{-2.0}$	$^{+15.0}_{-3.0}$	$^{+15.0}_{-3.0}$
CST efficiency	± 5.6	± 3.6	± 5.4	± 3.6
Lifetime tag	± 10.0			
Signal extraction	$^{+1.7}_{-0.4}$	$^{+4.9}_{-13.4}$	$^{+1.4}_{-12.1}$	$^{+3.7}_{-3.2}$
Branching fraction	± 6.7	± 2.3	± 24.7	± 2.3
Total systematic error	$^{+21.2}_{-16.0}$	$^{+16.5}_{-19.9}$	$^{+32.0}_{-31.8}$	$^{+20.0}_{-15.2}$

Table 2: *Percentage systematic errors on the inclusive cross sections for the different D mesons. Only the dominant contributions and the total error are shown.*

Cross section [nb]	D^+	D^0	D_s^+	D^{*+}
$\sigma_{vis}(ep \to eDX)$	2.16	6.53	1.67	2.90
Stat. error	± 0.19	± 0.49	± 0.41	± 0.20
Syst. error	$^{+0.46}_{-0.35}$	$^{+1.06}_{-1.30}$	$^{+0.54}_{-0.54}$	$^{+0.58}_{-0.44}$
AROMA LO prediction σ_{vis}	2.45	5.54	1.15	2.61
Prediction uncertainty	± 0.30	± 0.69	± 0.30	± 0.31
Estimated beauty contribution	10%	9%	17%	7%

Table 3: *Inclusive charmed meson electroproduction cross sections for the four meson states in the visible kinematic range, defined by $2 \leq Q^2 \leq 100\,\mathrm{GeV}^2$, $0.05 \leq y \leq 0.7$, $p_t(D) \geq 2.5\,\mathrm{GeV}$ and $|\eta(D)| \leq 1.5$. Also given are the predictions for D meson production (including the beauty contribution) based on a LO Monte Carlo simulation.*

Fragmentation factors	D^+	D^0	D_s^+	D^{*+}
$f(c \to D)$	0.202	0.658	0.156	0.263
Stat. error	± 0.020	± 0.054	± 0.043	± 0.019
Syst. error	$^{+0.045}_{-0.033}$	$^{+0.117}_{-0.142}$	$^{+0.036}_{-0.035}$	$^{+0.056}_{-0.042}$
Theo. error	$^{+0.029}_{-0.021}$	$^{+0.086}_{-0.048}$	$^{+0.050}_{-0.046}$	$^{+0.031}_{-0.022}$
$f_{\rm constraint}(c \to D)$	0.203	0.560	0.151	0.263
Total error	± 0.026	± 0.046	± 0.055	± 0.032
$f_{\rm wa}(c \to D)$	0.232 ± 0.018	0.549 ± 0.026	0.101 ± 0.027	0.235 ± 0.010

Table 4: *Fragmentation factors deduced from the measured cross sections. The small b contributions are subtracted. Also listed is the result of the constrained fit $f_{\rm constraint}(c \to D)$, its error (see text), and the world average numbers, given as $f_{\rm wa}(c \to D)$. The theoretical errors include the branching ratio uncertainty and the model dependences of the acceptance determination.*

Ratio	**this measurement**				e^+e^- **experiments**		
	value	stat.error	syst.error	theo.error	value	error	ref.
P_V^d	0.693	± 0.045	± 0.004	± 0.009	0.595	± 0.045	[42]
P_V^{u+d}	0.613	± 0.061	± 0.033	± 0.008	0.620	± 0.014	[43]
$R_{u/d}$	1.26	± 0.20	± 0.11	± 0.04	1.02	± 0.12	[42]
γ_s	0.36	± 0.10	± 0.01	± 0.08	0.31	± 0.07	[44]

Table 5: *Fragmentation characteristics derived according to equations 8-11 from the ratios of the fragmentation factors of table 4. Values measured by e^+e^- experiments are also quoted. The theoretical errors include the branching ratio uncertainty and the model dependences of the acceptance determination.*

$p_t(D^+)$ [GeV]	$\mathrm{d}\sigma_{vis}/\mathrm{d}p_t$ [nb/GeV]	errors [nb/GeV]				
		statistical	experimental		theoretical	
[2.5, 3.0]	1.95	± 0.32	$+0.41$	-0.34	$+0.13$	-0.14
[3.0, 3.5]	1.05	± 0.18	$+0.22$	-0.17	$+0.07$	-0.08
[3.5, 4.0]	0.556	± 0.128	$+0.121$	-0.090	$+0.039$	-0.039
[4.0, 5.0]	0.353	± 0.054	$+0.104$	-0.054	$+0.026$	-0.024
[5.0, 6.0]	0.063	± 0.023	$+0.072$	-0.010	$+0.004$	-0.005
[6.0, 10.0]	0.025	± 0.005	$+0.005$	-0.004	$+0.002$	-0.002

$\eta(D^+)$	$\mathrm{d}\sigma_{vis}/\mathrm{d}\eta$ [nb]	errors [nb]				
		statistical	experimental		theoretical	
[-1.50, -1.00]	0.84	± 0.16	$+0.25$	-0.12	$+0.06$	-0.08
[-1.00, -0.50]	0.97	± 0.15	$+0.20$	-0.14	$+0.07$	-0.07
[-0.50, 0.00]	0.66	± 0.12	$+0.14$	-0.10	$+0.05$	-0.04
[0.00, 0.50]	0.83	± 0.13	$+0.18$	-0.13	$+0.06$	-0.06
[0.50, 1.00]	0.76	± 0.15	$+0.36$	-0.22	$+0.06$	-0.05
[1.00, 1.50]	0.28	± 0.13	$+0.15$	-0.09	$+0.02$	-0.03

Q^2 [GeV^2]	$\mathrm{d}\sigma_{vis}/\mathrm{d}Q^2$ [$\mathrm{nb/GeV}^2$]	errors [$\mathrm{nb/GeV}^2$]				
		statistical	experimental		theoretical	
[2, 4]	0.200	± 0.038	$+0.047$	-0.033	$+0.014$	-0.015
[4, 7]	0.155	± 0.025	$+0.034$	-0.025	$+0.011$	-0.011
[7, 12]	0.095	± 0.015	$+0.021$	-0.014	$+0.008$	-0.007
[12, 22]	0.0373	± 0.0072	$+0.0105$	-0.0060	$+0.0025$	-0.0027
[22, 35]	0.0153	± 0.0036	$+0.0033$	-0.0026	$+0.0010$	-0.0012
[35, 100]	0.0042	± 0.0009	$+0.0009$	-0.0007	$+0.0003$	-0.0003

Table 6: *The bin-averaged single differential D^+ production cross section measurements $\sigma_{vis}(ep \to eD^+X)$ with statistical, experimental systematic and theoretical errors. The latter include the uncertainties of the branching ratio and the model dependence of the acceptance determination.*

$p_t(D^0)$ [GeV]	$d\sigma_{vis}/dp_t$ [nb/GeV]	errors [nb/GeV]				
		statistical	experimental		theoretical	
[2.5, 3.0]	5.29	± 0.72	$+1.11$	-0.89	$+0.13$	-0.18
[3.0, 3.5]	3.04	± 0.41	$+0.50$	-0.78	$+0.13$	-0.08
[3.5, 4.0]	2.29	± 0.34	$+0.81$	-0.62	$+0.09$	-0.06
[4.0, 5.0]	1.13	± 0.15	$+0.19$	-0.21	$+0.03$	-0.04
[5.0, 6.0]	0.516	± 0.120	$+0.139$	-0.129	$+0.018$	-0.015
[6.0, 10.0]	0.056	± 0.018	$+0.016$	-0.021	$+0.002$	-0.003

$\eta(D^0)$	$d\sigma_{vis}/d\eta$ [nb]	errors [nb]				
		statistical	experimental		theoretical	
[-1.50, -1.00]	1.85	± 0.38	$+0.34$	-0.46	$+0.09$	-0.05
[-1.00, -0.50]	1.74	± 0.30	$+0.28$	-0.28	$+0.04$	-0.07
[-0.50, 0.00]	2.43	± 0.34	$+0.42$	-0.36	$+0.06$	-0.11
[0.00, 0.50]	2.88	± 0.39	$+0.53$	-0.87	$+0.10$	-0.07
[0.50, 1.00]	2.67	± 0.37	$+0.52$	-0.87	$+0.10$	-0.07
[1.00, 1.50]	1.91	± 0.41	$+0.70$	-0.77	$+0.07$	-0.08

Q^2 [GeV^2]	$d\sigma_{vis}/dQ^2$ [$\mathrm{nb/GeV}^2$]	errors [$\mathrm{nb/GeV}^2$]				
		statistical	experimental		theoretical	
[2, 4]	0.662	± 0.099	$+0.113$	-0.161	$+0.024$	-0.019
[4, 7]	0.386	± 0.058	$+0.079$	-0.088	$+0.020$	-0.010
[7, 12]	0.267	± 0.043	$+0.066$	-0.057	$+0.008$	-0.007
[12, 22]	0.102	± 0.018	$+0.021$	-0.023	$+0.003$	-0.003
[22, 35]	0.0474	± 0.0113	$+0.0096$	-0.0107	$+0.0013$	-0.0013
[35, 100]	0.0186	± 0.0027	$+0.0032$	-0.0038	$+0.0005$	-0.0007

Table 7: *The bin-averaged single differential D^0 production cross section measurements $\sigma_{vis}(ep \to eD^0X)$ with statistical, experimental systematic and theoretical errors. The latter include the uncertainties of the branching ratio and the model dependence of the acceptance determination.*

$p_t(D_s^+)$ [GeV]	$\mathrm{d}\sigma_{vis}/\mathrm{d}p_t$ [nb/GeV]	errors [nb/GeV]				
		statistical	experimental		theoretical	
[2.5, 3.5]	1.09	± 0.33	$+0.22$	-0.27	$+0.27$	-0.27
[3.5, 4.0]	0.44	± 0.20	$+0.16$	-0.09	$+0.11$	-0.11
[4.0, 10.0]	0.071	± 0.021	$+0.016$	-0.012	$+0.018$	-0.018

$\eta(D_s^+)$	$\mathrm{d}\sigma_{vis}/\mathrm{d}\eta$ [nb]	errors [nb]				
		statistical	experimental		theoretical	
[-1.50, -0.50]	0.59	± 0.19	$+0.12$	-0.10	$+0.15$	-0.15
[-0.50, 0.75]	0.50	± 0.17	$+0.10$	-0.12	$+0.12$	-0.12
[0.75, 1.50]	0.81	± 0.25	$+0.43$	-0.29	$+0.20$	-0.21

Q^2 [GeV^2]	$\mathrm{d}\sigma_{vis}/\mathrm{d}Q^2$ [$\mathrm{nb/GeV}^2$]	errors [$\mathrm{nb/GeV}^2$]				
		statistical	experimental		theoretical	
[2, 6]	0.172	± 0.044	$+0.048$	-0.038	$+0.043$	-0.043
[6, 16]	0.053	± 0.017	$+0.012$	-0.012	$+0.013$	-0.013
[16, 100]	0.0065	± 0.0028	$+0.0014$	-0.0013	$+0.0016$	-0.0016

Table 8: *The bin-averaged single differential D_s^+ production cross section measurements $\sigma_{vis}(ep \to eD_s^+X)$ with statistical, experimental systematic and theoretical errors. The latter include the uncertainties of the branching ratio and the model dependence of the acceptance determination.*

$p_t(D^{*+})$ [GeV]	$d\sigma_{vis}/dp_t$ [nb/GeV]	errors [nb/GeV]				
		statistical	experimental		theoretical	
[2.5, 3.0]	2.31	± 0.28	$+0.50$	-0.40	$+0.07$	-0.06
[3.0, 3.5]	1.15	± 0.16	$+0.23$	-0.19	$+0.03$	-0.04
[3.5, 4.0]	1.03	± 0.13	$+0.21$	-0.16	$+0.03$	-0.03
[4.0, 5.0]	0.344	± 0.055	$+0.085$	-0.055	$+0.011$	-0.009
[5.0, 6.0]	0.224	± 0.041	$+0.048$	-0.037	$+0.006$	-0.009
[6.0, 10.0]	0.027	± 0.007	$+0.015$	-0.004	$+0.001$	-0.001

$\eta(D^{*+})$	$d\sigma_{vis}/d\eta$ [nb]	errors [nb]				
		statistical	experimental		theoretical	
[-1.50, -1.00]	0.62	± 0.13	$+0.14$	-0.09	$+0.02$	-0.02
[-1.00, -0.50]	1.10	± 0.13	$+0.23$	-0.14	$+0.03$	-0.03
[-0.50, 0.00]	1.20	± 0.14	$+0.24$	-0.15	$+0.03$	-0.03
[0.00, 0.50]	1.15	± 0.16	$+0.22$	-0.20	$+0.03$	-0.04
[0.50, 1.00]	0.99	± 0.15	$+0.23$	-0.31	$+0.03$	-0.02
[1.00, 1.50]	0.65	± 0.16	$+0.32$	-0.25	$+0.03$	-0.02

Q^2 [GeV^2]	$d\sigma_{vis}/dQ^2$ [$\mathrm{nb/GeV}^2$]	errors [$\mathrm{nb/GeV}^2$]				
		statistical	experimental		theoretical	
[2, 4]	0.359	± 0.043	$+0.079$	-0.062	$+0.014$	-0.009
[4, 7]	0.193	± 0.027	$+0.045$	-0.036	$+0.005$	-0.006
[7, 12]	0.107	± 0.014	$+0.021$	-0.015	$+0.003$	-0.004
[12, 22]	0.0486	± 0.0068	$+0.0109$	-0.0084	$+0.0014$	-0.0013
[22, 35]	0.0180	± 0.0038	$+0.0036$	-0.0026	$+0.0005$	-0.0007
[35, 100]	0.0064	± 0.0010	$+0.0013$	-0.0009	$+0.0002$	-0.0002

Table 9: *The bin-averaged single differential D^{*+} production cross section measurements $\sigma_{vis}(ep \to eD^{*+}X)$ with statistical, experimental systematic and theoretical errors. The latter include the uncertainties of the branching ratio and the model dependence of the acceptance determination. The D^{*+} tagged D^0 signals used for the measurement fulfill life time tagging requirements.*